

Structural mechanism of cGAS inhibition by nucleosomes

2

3 Ganesh R. Pathare^{1,2,9}, Alexiane Decout^{3,9}, Selene Glück³, Simone Cavadini^{1,2}, Kristina Makasheva⁴,
4 Ruud Hovius⁴, Georg Kempf^{1,2}, Joscha Weiss^{1,2}, Zuzanna Kozicka^{1,2}, Baptiste Guey³,
5 Pauline Melenec³, Beat Fierz⁴, Nicolas H. Thomä^{1,2*}, Andrea Ablasser^{3*}

6

7 ¹Friedrich Miescher Institute for Biomedical Research, Basel, Switzerland.

8 ²University of Basel, Basel, Switzerland.

9 ³Global Health Institute, Swiss Federal Institute of Technology Lausanne (EPFL), Switzerland.

10 ⁴Institute of Chemical Sciences and Engineering, Swiss Federal Institute of Technology Lausanne
11 (EPFL), Switzerland. □

12

13

14 ⁹*These authors contributed equally to this work.*

15 *email: andrea.ablasser@epfl.ch and nicolas.thoma@fmi.ch

16

17 The DNA sensor cGAS initiates innate immune responses following microbial
18 infection, cellular stress, and cancer [1]. Upon activation by double-stranded DNA,
19 cytosolic cGAS produces 2'3' cyclic GMP-AMP and triggers inflammatory cytokine
20 and type I interferon (IFN) induction [2-7]. cGAS is also present inside the cell nucleus
21 replete with genomic DNA [8], where chromatin has been implicated in restricting its
22 enzymatic activity [9]. However, the structural basis for cGAS inhibition by chromatin
23 has remained unknown. Here we present the cryo-electron microscopy structure of
24 human cGAS bound to nucleosomes at 3.1 Å resolution. cGAS makes extensive
25 contacts with both the acidic patch of the histone H2A-H2B heterodimer and
26 nucleosomal DNA. The structural and complementary biochemical analysis also finds
27 cGAS engaged to a second nucleosome *in trans*. Mechanistically, nucleosome
28 binding locks cGAS in a monomeric state, in which steric hindrance suppresses
29 spurious activation by genomic DNA. We find that mutations to the cGAS-acidic patch
30 interface are necessary and sufficient to abolish the inhibitory effect of nucleosomes
31 *in vitro* and to unleash cGAS activity on genomic DNA in living cells. Our work
32 uncovers the structural basis of cGAS interaction with chromatin and defines a
33 compelling mechanism that permits self-nonsel discrimination of genomic DNA by
34 cGAS.

35

36 In the cytoplasm of mammalian cells, the enzyme cGAS is crucial for the detection of
37 double-stranded DNA (dsDNA) during infection [2]. On binding dsDNA, cGAS synthesises
38 the second messenger 2'3' cyclic GMP-AMP (cGAMP), which in turn stimulates antiviral and
39 pro-inflammatory responses through the adaptor protein STING [2-7, 10]. In addition, a pool
40 of cGAS is also present inside the cellular nucleus strongly associating with chromatin [8, 9,
41 11]. The chromatinised state of intact genomic DNA has been reported to limit cGAS activity
42 [12, 13], and cGAS has been found to bind nucleosomes tighter than the corresponding
43 naked DNA duplexes [13]. Here we sought a mechanism that explains how cGAS can be
44 juxtaposed to nucleosomal DNA without undergoing activation.

45

46 **H2A-H2B is the minimal inhibitory histone unit for cGAS**

47 We tested whether histones, the building blocks of nucleosomes, may regulate cGAS inside
48 the nucleus. Treatment of cells with aclarubicin robustly evicts core histones from chromatin
49 [14], in particular histone H2A and H2B (**Extended Data Fig. 1b**). Interestingly, disruption of
50 nucleosomes by aclarubicin also led to mobilization of nuclear cGAS (**Extended Data Fig.**
51 **1b**). Proximity-ligation assays (PLA) further indicated prominent associations of cGAS with

52 histones *in situ*, which were partially lost upon aclarubicin treatment (**Extended Data Fig.**
53 **1c, d**). Thus, histones appear to dynamically engage cGAS in the nucleus.

54 Consistent with prior work [13], functional analysis of cGAS *in vitro* enzymatic activity
55 revealed that mononucleosomes (hereafter nucleosomes) inhibited DNA-induced cGAMP
56 synthesis (**Extended Data Fig. 1e**). Likewise, compact chromatin fibres (12-mer
57 nucleosome arrays) suppressed cGAS activity (**Extended Data Fig. 1e**). H2A-H2B dimers
58 also had an inhibitory effect, but neither H2A or H2B monomers nor H3 or H4 monomers,
59 respectively (**Extended Data Fig. 1f, g**). Thus, H2A-H2B dimers on their own can suppress
60 cGAS (**Extended Data Fig. 1h**), albeit with weaker overall potency compared to full-
61 assembled nucleosomes with additional features of nucleosomes in chromatin being
62 necessary to exert maximal inhibition.

63

64 **Overall structure of the cGAS-NCP complex**

65 To determine how cGAS interacts with nucleosomes, we pursued structural studies. A 1.5:1
66 molar mixture of human cGAS (residues 155 to 522) with a 147 bp 601 DNA nucleosome
67 core particle (NCP) resulted in heterogenous particle distributions (**Extended Data Fig. 2a-**
68 **d**). To select for and stabilize more homogenous cGAS-NCP complexes, we combined
69 gradient centrifugation with chemical crosslinking (GraFix) [15]. Both WT cGAS and cGAS
70 K394E, a mutant impaired in dsDNA-mediated cGAS dimerisation [16], were used for
71 structure determination. For the cGAS K394E mutant, we obtained a 4.1 Å reconstruction
72 revealing two NCPs organized in a NCP₁-cGAS₁-cGAS₂-NCP₂ sandwich arrangement with
73 an expected molecular weight around 560 kDa, consistent with the most prominent peak
74 fraction in multi-angle light scattering (MALS) (**Fig. 1a, b, Extended Data Fig. 3,**
75 **Supplementary Video 1, 2, and Extended Data Table 1a**). The two individual nucleosomes
76 are held together by two cGAS protomers. While the first cGAS protomer and its
77 corresponding NCP (designated cGAS₁ and NCP₁) are well-resolved, the second
78 nucleosome/cGAS pair (NCP₂ and cGAS₂) is less ordered (**Extended Data Fig. 3e**). In the
79 dimeric NCP₁-cGAS₁-cGAS₂-NCP₂ arrangement, each cGAS protomer interacts with the
80 histone octamer of one NCP through histones H2A and H2B and the nucleosomal DNA (e.g.
81 cGAS₁ and NCP₁), while contacting the second nucleosome (e.g. cGAS₁ and NCP₂) primarily
82 through interactions with the nucleosomal DNA (**Fig. 1a, b**). In the WT cGAS structure, we
83 observed a similar overall structural arrangement, with the NCP₁-cGAS₁-cGAS₂-NCP₂
84 complex at 5.1Å and the focused NCP₁-cGAS₁ structure at 4.7Å resolution (**Extended Data**
85 **Fig. 4, 5; Extended Data Table 1**). Given the structural similarity, the higher resolution
86 cGAS K394E mutant was used for subsequent analysis (**Extended Data Fig. 3** and
87 **Extended Data Fig. 6**).

88 **Structural insights into the cGAS₁-NCP₁ complex**

89 Focused 3D classification of cGAS₁-NCP₁ yielded a structure at a resolution of 3.1 Å (**Fig.**
90 **1c**, **Extended Data Fig. 3c, f** and **Extended Data Table 1a**). This revealed the binding
91 interfaces between cGAS and the nucleosome, which is in large parts contributed by three
92 contact surfaces on cGAS interacting with the acidic patch of H2A-H2B—a common site
93 involved in protein-nucleosome assemblies [17] (**Fig. 2a**, **Extended Data Fig. 6a-d** and
94 **Supplementary Video 3**): (i) Loop1(residues 234-237), a canonical acidic patch contact
95 involving cGAS R236 salt-bridging to H2A E62 and E65 (**Fig. 2a** and **Extended Data Fig.**
96 **6b**); (ii) Loop2 (residues 255 to 258), a proximal cGAS loop connecting β4 and α4, with
97 R255 salt-bridging H2A residues D91, E93 and E62 (**Fig. 2a** and **Extended Data Fig. 6c**);
98 (iii) Loop3 (residues 328 to 330) that together with the C-terminal end of cGAS helix α5 (354-
99 356) forms multiple interactions with H2A helix α3 (residues 64-71)(**Fig. 2a** and **Extended**
100 **Data Fig. 6d**). In addition to these protein-protein interactions, the cGAS₁ C-lobe also forms
101 localised DNA backbone contacts with NCP₁ engaging the nucleosomal DNA around super-
102 helical location (SHL) 6 through residues K347 and K350 (**Fig. 2a** (right panel) and
103 **Extended Data Fig. 6e, f**) [18].

104 To dissect the functional importance of the observed cGAS interfaces with NCP₁, we
105 performed site-directed mutagenesis and carried out electromobility shift assays (EMSA).
106 Mutation of cGAS residues that engage the nucleosomal acidic patch (R255A, R236A)
107 completely abrogated nucleosome binding (**Fig. 2b**). In *in vitro* enzymatic activity, we found
108 that both cGAS R255A and cGAS R236A were no longer inhibited by chromatin (**Fig. 2c**).
109 To corroborate the relevance of the acidic patch interaction for cGAS inhibition, we made
110 use of a peptide derived from the latency-associated nuclear antigen (LANA), a well-known
111 acidic patch binder [19]. In the presence of the LANA peptide, but not a corresponding
112 mutant peptide, cGAS was competed off from the nucleosome and regained *in vitro* DNA-
113 induced activity in the presence of chromatin as judged by robust cGAMP synthesis
114 (**Extended Data Fig. 7a, b**). Of note, cGAS residues K350 and L354, which contacts the
115 nucleosomal DNA of NCP₁ (**Extended Data Fig. 6f, i**), also had significant effects on
116 nucleosome binding and inhibition when mutated (**Fig. 2 d, e** and **Extended Data Fig. 6f, i**).
117 Thus, cGAS is anchored to chromatin through a bipartite interface on nucleosomes
118 composed of the acidic patch and nucleosomal DNA contacts, respectively.

119

120 **Mechanism of cGAS inhibition by NCP₁**

121 In canonical binding of dsDNA, two separate surfaces on cGAS, designated A-site and B-
122 site respectively, interact with two individual strands of DNA to promote the assembly of a
123 2:2 cGAS:DNA complex – the minimal active enzymatic unit [20-23] (**Fig. 2f**). Moreover, a

124 third DNA binding site, designated C-site, has been implicated to facilitate cGAS
125 oligomerization in liquid-phase condensation [24]. In the NCP-bound configuration, the
126 cGAS A-site including the Zn-thumb faces the histone octamer disc. Nucleosomal DNA
127 interactions are further enforced by residues essential for cGAS dimerisation (e.g. K394)
128 (**Extended Data Fig. 4c, d**), although the K394-containing loop and the zinc-finger motif
129 play only a minor role in nucleosome binding (**Extended Data Fig. 4c, d** and **Extended**
130 **Data Fig. 7f-g**). The key cGAS-NCP interaction originate from the B-site (e.g. R236, K254,
131 S328), which also contributes to nucleosomal DNA binding (e.g., K347, L354). The cGAS
132 active site in our structure points away from NCP₁ towards the solvent and NCP₂ and is
133 principally accessible (**Fig. 2**).

134 Nucleosome binding hence confers cGAS inactivation in three essential ways (**Fig.**
135 **2g, h** and **Supplementary Video 4**): first, owing to steric clashes with both the nucleosomal
136 DNA as well as histones H2A and H2B, cGAS cannot engage dsDNA at the interface
137 between lobe1 and 2; second, key residues on cGAS required for DNA binding and
138 dimerisation are tied up in interactions with the nucleosome and, thus, are not available for
139 canonical dsDNA binding and activation (**Extended Data Fig. 4c, d**); third, both histones
140 and nucleosomal DNA sterically prevent cGAS dimerisation, an essential prerequisite for
141 enzymatic activity [16, 21, 22]. Importantly, the steric restrictions imparted by H2A-H2B are
142 sufficiently pronounced to explain the inability of cGAS to undergo dsDNA-dependent
143 activation in the presence of this histone dimer. The structure hence provides the
144 mechanism of cGAS inhibition by H2A-H2B, while identifying additional contacts and
145 inhibitory principles specific to cGAS inhibition by nucleosomes (**Extended Data Fig. 6g-i**).

146 We next dissected the contributions of nucleosomal DNA versus linker DNA to cGAS
147 binding and activation. Fluorescence polarization assays revealed that cGAS binds tighter to
148 nucleosomes with long overhangs than to those without or with only short overhangs, likely
149 due to the presence of additional DNA-binding sites (**Extended Data Fig. 7d, e**). We then
150 assessed the catalytic activity of cGAS (WT) and cGAS acidic patch mutants, R236A and
151 R255A, on nucleosomes with and without a 80bp dsDNA overhang. Whereas cGAS (WT)
152 and cGAS mutants robustly synthesized cGAMP on naked dsDNA, they remained inactive in
153 the presence of nucleosomes lacking a DNA overhang (**Extended Data Fig. 7c**).
154 Nucleosomal DNA is thus not a good substrate for cGAS activation. Nucleosomes carrying
155 80bp long linker DNA still failed to activate WT cGAS, but elicited activation of both cGAS
156 R236A and R255A (**Extended Data Fig. 7c**). Thus, *in vitro* cGAS (WT) preferentially binds
157 to NCP over linker DNA limiting its enzymatic activity.

158 ***In trans* interaction between cGAS and NCP₂**

159 The cGAS₁ protomer also binds a second nucleosome (e.g. cGAS₁ and NCP₂)
160 predominantly through protein-DNA contacts with the nucleosomal DNA at SHL 3. The two
161 NCPs are held ~20 Å apart with the DNA entry/exit sites of the two nucleosomes pointing
162 roughly ~90° away (**Fig. 3a**). The interaction with the second nucleosome is mediated by
163 phosphate backbone contacts involving conserved cGAS₁ residues E287, K299-R302, and
164 K427 (**Fig. 3b**). Compared to the protein-DNA contacts, fewer and less well ordered
165 cGAS₁/NCP₂ protein-protein interactions were observed between a β-hairpin loop (cGAS
166 residues 365-369) extending towards the C-terminal tail of the H2B, as well as inter-
167 nucleosomal contacts between two N-terminal tails of histone H4 (**Extended Data Fig. 8a,**
168 **b**). The *in trans* nucleosome interaction interface on cGAS is largely provided by the C-site
169 (**Extended Data Fig.8c-f**)[24], which in this structure supports higher-order cGAS/NCP
170 assemblies.

171 To validate the observed *in trans* cGAS₁/NCP₂ interface, we performed EMSA assays.
172 We found that the combined mutation of the NCP₂ interacting motifs on cGAS (K285, R300
173 and K427) still allowed for cGAS interaction with nucleosomes, as indicated by a prominent
174 EMSA gel shift likely reflecting a 1:1 cGAS₁/NCP₁ complex (**Fig. 3c**). However, all higher-
175 order cGAS/NCP assemblies readily detected with cGAS (WT) were lost when mutating the
176 secondary nucleosome binding site. Consistent with the preserved ability to bind
177 nucleosome *in vitro*, mutations to the cGAS *in trans* interface (K285A/R300A/K427A) had no
178 detectable effect on cGAS intranuclear tethering in reconstituted HeLa cGAS KO cells
179 (**Extended Data Fig. 8g**). Hence, whilst the bipartite cGAS/NCP₁ interface forms the primary
180 anchoring motif between cGAS and the nucleosome, the secondary cGAS₁/NCP₂ interface
181 critically contributes to the formation of higher-order complexes.

182

183 **Impact of structure-based mutations on cellular activity**

184 To determine the functional relationship between nucleosome binding and cGAS inhibition in
185 cells, we focused on motifs on cGAS that interact with the acidic patch (R255A, R236A)
186 (**Fig. 4a-c**) and with the nucleosomal DNA *in cis* (i.e. NCP₁-cGAS₁; K350A, L354A), the two
187 key *in vitro* interfaces for cGAS nucleosome binding (**Fig. 2a**). Consistent with our *in vitro*
188 assays and extending recent work [9], cGAS mutants R236A and R255A as well as
189 K350A/L354A were strongly defective in nuclear tethering when expressed in cGAS KO
190 HeLa cells (**Fig. 4d**). Using fluorescence recovery after photobleaching (FRAP), we detected
191 differences between the mutants in their degree of intranuclear mobility with cGAS R255A
192 showing highest, R236A intermediate, and K350A/L354A lowest mobility relative to WT
193 cGAS, respectively (**Fig. 4e** and **Extended Data Fig. 9a**). Interestingly, the degree of
194 dissociation correlated well with cellular cGAS responses with R255A expression triggering

195 highest cGAMP levels, followed by R236A, and cGAS K350/L354A showing negligible
196 activity (**Fig. 4f**).

197 We next examined whether expression of the two most striking cGAS mutants, R236A
198 and R255A, stimulates a type I IFN response. Activation of cGAS not only promotes
199 conventional, cell-autonomous signalling, but elicits cellular activation also *in trans* through
200 the transfer of cGAMP [25]. We found that cGAS mutants triggered only modest
201 upregulation of interferon-stimulated genes (ISGs) when induced in a synchronized manner
202 in mono-cultures of HeLa cells (**Extended Data Fig. 9b**). An effect that may be due to
203 negative feedback regulation at the level of STING [26, 27] resulting in non-responsiveness
204 toward intracellular cGAMP accumulation over time (**Extended Data Fig. 9c, d**). By
205 contrast, in co-culture with human BJ fibroblasts serving as naive acceptor cells, the
206 expression of cGAS mutants in HeLa cells induced strong ISG upregulation and WT cGAS
207 had no such effect (**Fig. 4g**). Collectively these findings suggest that disrupting the
208 interaction of cGAS with the acidic patch of nucleosomes is in itself sufficient to trigger
209 innate immune activation.

210

211 Discussion

212 We provide the structural basis for cGAS inhibition by nucleosomes: a bipartite interface
213 involving contacts to both the acidic patch of H2A-H2B dimers and the nucleosomal DNA
214 “traps” cGAS in an inactive state, in which cGAS can neither engage dsDNA in a manner
215 required for canonical dsDNA sensing nor undergo the dimerisation/oligomerisation reaction
216 required for its catalytic activity.

217 Based on our work, we propose that cGAS uses a “missing-self” recognition strategy
218 to reliably discriminate between self- and non-self DNA: instead of focusing on pathogen-
219 specific features that promote activation as is the case for many pattern recognition
220 receptors [28], cGAS exploits the suppressive activity of nucleosomes, leveraging essentially
221 “inbuilt identifiers” of eukaryotic genomes, to avert aberrant activity. The motifs responsible
222 for cGAS interactions with the nucleosome are well-conserved within cGAS homologs that
223 utilize DNA for the regulation of their catalytic activity (**Extended Data Fig. 9e**). We propose
224 that the inhibitory interaction of cGAS with nucleosomes is a key element of a multi-layered
225 regulation strategy allowing cGAS to reside in the nucleus without undergoing persistent
226 activation [29].

227

228

229 References

- 230 1. Ablasser, A. and Z.J. Chen, *cGAS in action: Expanding roles in immunity and*
231 *inflammation*. Science, 2019. **363**(6431).
- 232 2. Sun, L., et al., *Cyclic GMP-AMP synthase is a cytosolic DNA sensor that activates*
233 *the type I interferon pathway*. Science, 2013. **339**(6121): p. 786-91.
- 234 3. Wu, J., et al., *Cyclic GMP-AMP is an endogenous second messenger in innate*
235 *immune signaling by cytosolic DNA*. Science, 2013. **339**(6121): p. 826-30.
- 236 4. Ablasser, A., et al., *cGAS produces a 2'-5'-linked cyclic dinucleotide second*
237 *messenger that activates STING*. Nature, 2013. **498**(7454): p. 380-4.
- 238 5. Gao, P., et al., *Cyclic [G(2',5')pA(3',5')p] is the metazoan second messenger*
239 *produced by DNA-activated cyclic GMP-AMP synthase*. Cell, 2013. **153**(5): p. 1094-
240 107.
- 241 6. Diner, E.J., et al., *The innate immune DNA sensor cGAS produces a noncanonical*
242 *cyclic dinucleotide that activates human STING*. Cell Rep, 2013. **3**(5): p. 1355-61.
- 243 7. Zhang, X., et al., *Cyclic GMP-AMP containing mixed phosphodiester linkages is an*
244 *endogenous high-affinity ligand for STING*. Mol Cell, 2013. **51**(2): p. 226-35.
- 245 8. Gentili, M., et al., *The N-Terminal Domain of cGAS Determines Preferential*
246 *Association with Centromeric DNA and Innate Immune Activation in the Nucleus*. Cell
247 Rep, 2019. **26**(13): p. 3798.
- 248 9. Volkman, H.E., et al., *Tight nuclear tethering of cGAS is essential for preventing*
249 *autoreactivity*. Elife, 2019. **8**.
- 250 10. Barber, G.N., *STING: infection, inflammation and cancer*. Nat Rev Immunol, 2015.
251 **15**(12): p. 760-70.
- 252 11. Orzalli, M.H., et al., *cGAS-mediated stabilization of IFI16 promotes innate signaling*
253 *during herpes simplex virus infection*. Proc Natl Acad Sci U S A, 2015. **112**(14): p.
254 E1773-81.
- 255 12. Lahaye, X., et al., *NONO Detects the Nuclear HIV Capsid to Promote cGAS-*
256 *Mediated Innate Immune Activation*. Cell, 2018. **175**(2): p. 488-501 e22.
- 257 13. Zierhut, C., et al., *The Cytoplasmic DNA Sensor cGAS Promotes Mitotic Cell Death*.
258 Cell, 2019. **178**(2): p. 302-315 e23.
- 259 14. Pang, B., et al., *Drug-induced histone eviction from open chromatin contributes to the*
260 *chemotherapeutic effects of doxorubicin*. Nat Commun, 2013. **4**: p. 1908.
- 261 15. Stark, H., *GraFix: stabilization of fragile macromolecular complexes for single particle*
262 *cryo-EM*. Methods Enzymol, 2010. **481**: p. 109-26.
- 263 16. Li, X., et al., *Cyclic GMP-AMP synthase is activated by double-stranded DNA-*
264 *induced oligomerization*. Immunity, 2013. **39**(6): p. 1019-31.
- 265 17. McGinty, R.K. and S. Tan, *Nucleosome structure and function*. Chem Rev, 2015.
266 **115**(6): p. 2255-73.

- 267 18. Civril, F., et al., *Structural mechanism of cytosolic DNA sensing by cGAS*. Nature,
268 2013. **498**(7454): p. 332-7.
- 269 19. Barbera, A.J., et al., *The nucleosomal surface as a docking station for Kaposi's*
270 *sarcoma herpesvirus LANA*. Science, 2006. **311**(5762): p. 856-61.
- 271 20. Abe, T. and G.N. Barber, *Cytosolic-DNA-mediated, STING-dependent*
272 *proinflammatory gene induction necessitates canonical NF-kappaB activation*
273 *through TBK1*. J Virol, 2014. **88**(10): p. 5328-41.
- 274 21. Zhang, X., et al., *The cytosolic DNA sensor cGAS forms an oligomeric complex with*
275 *DNA and undergoes switch-like conformational changes in the activation loop*. Cell
276 Rep, 2014. **6**(3): p. 421-30.
- 277 22. Andreeva, L., et al., *cGAS senses long and HMGB/TFAM-bound U-turn DNA by*
278 *forming protein-DNA ladders*. Nature, 2017. **549**(7672): p. 394-398.
- 279 23. Zhou, W., et al., *Structure of the Human cGAS-DNA Complex Reveals Enhanced*
280 *Control of Immune Surveillance*. Cell, 2018. **174**(2): p. 300-311 e11.
- 281 24. Xie, W., et al., *Human cGAS catalytic domain has an additional DNA-binding*
282 *interface that enhances enzymatic activity and liquid-phase condensation*. Proc Natl
283 Acad Sci U S A, 2019.
- 284 25. Ablasser, A., et al., *Cell intrinsic immunity spreads to bystander cells via the*
285 *intercellular transfer of cGAMP*. Nature, 2013. **503**(7477): p. 530-4.
- 286 26. Dobbs, N., et al., *STING Activation by Translocation from the ER Is Associated with*
287 *Infection and Autoinflammatory Disease*. Cell Host Microbe, 2015. **18**(2): p. 157-68.
- 288 27. Konno, H., K. Konno, and G.N. Barber, *Cyclic dinucleotides trigger ULK1 (ATG1)*
289 *phosphorylation of STING to prevent sustained innate immune signaling*. Cell, 2013.
290 **155**(3): p. 688-98.
- 291 28. Janeway, C.A., Jr., *Approaching the asymptote? Evolution and revolution in*
292 *immunology*. Cold Spring Harb Symp Quant Biol, 1989. **54 Pt 1**: p. 1-13.
- 293 29. Ablasser, A. and S. Hur, *Regulation of cGAS- and RLR-mediated immunity to nucleic*
294 *acids*. Nat Immunol, 2020. **21**(1): p. 17-29.

295

296 **Author contributions** G.R.P. conducted the cryo-EM experiments and data processing with
297 help from S.C. and G.K. for the model building. A.D. performed *in vitro* assays and purified
298 recombinant cGAS. S.G., P.M. and A.A. performed cellular experiments. K.M. and R.H.
299 purified recombinant histone proteins and assembled the recombinant nucleosomes and
300 chromatin fibers. EM samples were prepared by G.R.P with help from J.W.. Z.K. and J.W
301 performed fluorescence polarization assays. B.G. performed FRAP experiments. B.F.
302 supervised experiments related to the *in vitro* reconstitution of nucleosomes/chromatin and
303 provided valuable discussion. N.T. supervised the structural work and the biophysical

304 assays. A.A. supervised the *in vitro* assays and cellular studies. N.T. and A.A. wrote the
305 manuscript with input from all authors.

306

307 **Acknowledgments** We thank Nathalie Jordan and Jonathan Ricci for technical assistance.
308 Funding: A.A. received grants from the SNF (BSSGI0-155984, 31003A_159836), NCCR in
309 Chemical Biology, and was supported by the European Union's Horizon 2020 Research and
310 Innovation program grant agreement (grant no: 804933, ImAgine). N.H.T. was
311 supported by the European Research Council (ERC) under the European Union's Horizon
312 2020 Research and Innovation program grant agreement (grant no. 666068), the Novartis
313 Research Foundation and by the SNF (31003A_179541). B.F. is supported by the European
314 Union's Horizon 2020 Research and Innovation program grant agreement (grant no:
315 724022, chromo-SUMMIT) and the NCCR in Chemical Biology. Z.K. was supported by the
316 European Union's Horizon 2020 Research and Innovation Program under the Marie
317 Skłodowska-Curie grant agreement no. 765445.

318

319 **Data availability** The electron density reconstructions and corresponding final models for
320 NCP₁-cGAS₁ -cGAS₂-NCP₂, and NCP₁-cGAS₁ were deposited in the EM Data Base
321 (accession code: EMDB- 10694 and EMDB-10695) and in the Protein Data Bank (accession
322 code: 6Y5D and 6Y5E). The electron density reconstructions for NCP₁-WTcGAS₁-
323 WTcGAS₂-NCP₂ and NCP₁-WTcGAS₁ were deposited in the EM Data Base (accession
324 code: EMDB- 11006 and EMDB-11005).

325

326 **Competing interests** A.A. is a member of the scientific advisory board of IFM Therapeutics
327 and scientific co-founder of IFM-Due.

328

329 **Correspondence and requests for materials** should be addressed to N.H.T. or A.A.

330

331

332

333 **Figure legends**

334

335

336 **Fig. 1 | Cryo-EM structure of cGAS bound to nucleosomes.**

337 **a**, 3D reconstruction of the complex containing two cGAS protomers, cGAS1 (red) and
 338 cGAS2 (orange), and two nucleosomal core particles, NCP1 and NCP2, respectively. **b**, **c**,
 339 Ribbon diagram of NCP₁-cGAS₁-cGAS₂-NCP₂ complex (**b**) and cGAS₁-NCP₁ complex (**c**) fit
 340 into corresponding electron-density maps. The two lobes of cGAS, N-lobe and C-lobe,
 341 respectively, are shown in pink and red. **d**, Schematic domain architecture for human cGAS
 342 (hcGAS) as previously defined [23]. Residue numbers are shown and the dotted line
 343 indicates the construct used for structural analysis. dsDNA sensing regions involved in
 344 cGAS activation are underlined in purple and nucleosome binding regions involved in cGAS
 345 inhibition are marked by blue boxes.

346

347 **Fig. 2 | The cGAS₁-NCP₁ complex and structural mechanism of inhibition.**

348 **a**, Magnified view of the cGAS₁(K394E)-NCP₁ complex bipartite interactions, cGAS-histone
 349 interactions (left) and cGAS-nucleosomal DNA interactions (right). **b**, EMSA gel showing the
 350 interaction of nucleosomes (40 ng/μl) with a concentration gradient of WT, R255A cGAS,
 351 and R236A cGAS (from 50 ng/μl to 6 ng/μl; 1:2 step dilutions); black arrows indicate higher-
 352 order cGAS NCP complexes. **c**, *In vitro* cGAMP synthesis of WT, R255A cGAS, and R236A
 353 cGAS with or without a concentration gradient of chromatin (from 5 nM to 0.3125 nM; 1:2
 354 step dilutions) normalized by cGAMP levels in absence of chromatin for each individual
 355 mutant. **d**, EMSA gel showing the interaction of nucleosomes (40 ng/μl) with increasing
 356 concentrations of WT or K350A/L354A cGAS (from 100 ng/μl to 12 ng/μl; 1:2 step dilution).
 357 **e**, *In vitro* cGAMP synthesis of WT and K350A/L354A hcGAS with or without chromatin (5
 358 nM) normalized by cGAMP levels in absence of chromatin for each individual mutant. Data
 359 are representative for three independent experiments showing similar results (**b**, **d**) or mean
 360 ± s.d. of $n = 3$ independent experiments (**c**, **e**) is shown. One-way ANOVA with post hoc
 361 Dunnett multiple comparison test; $P = 0.0092$ (**), $P = 0.092$ (*) (WT), and $P = 0.0311$ (*)
 362 (R236A) and (**c**) and two-tailed student's t -test; $P = 0.0192$ (*) (**e**). Data points are from
 363 experimentally independent experiments. **f**, Overview of active hcGAS-DNA 2:2 complex
 364 with two distinct dsDNA-binding surfaces (A-site and B-site)[16] (PDB: 4LEY). **g**,
 365 Superposition of the hcGAS-dsDNA (**f**) and cGAS₁-NCP₁ complex illustrating the
 366 incompatibility of DNA ligand binding (dsDNA1 in yellow) to cGAS in the nucleosome-bound
 367 configuration. **h**, Model based on superpositioning the cGAS₁-NCP₁ complex onto DNA-
 368 bound cGAS oligomers as previously defined [22] (PDB: 5N6I)(**h**). For gel source data, see
 369 Supplementary Figure 1.

370

371 **Fig. 3 | cGAS interactions with the second nucleosome *in trans*.**

372 **a, b**, The NCP₁-cGAS₁-cGAS₂-NCP₂ di-nucleosomal arrangement is shown. Magnified view
373 detailing the interactions between the N-lobe of cGAS₁ (pink), the C-lobe of cGAS₁ (red) and
374 the nucleosomal DNA of NCP₂ (grey) (**b** below). **c**, EMSA gel showing the interaction of
375 nucleosomes with increasing concentrations of WT or K285A/R300A/K427A cGAS (100
376 ng/μl to 12 ng/μl; 1:2 step dilution). Arrowheads highlighting free nucleosomes (dark grey),
377 complexed nucleosomes (black), and a putative 1:1 cGAS:NCP assembly (light grey). The
378 experiment shown in **c** was independently repeated three times with similar results. For gel
379 source data, see Supplementary Figure 1.

380

381 **Fig. 4 | Impact of structure-based mutations on cellular cGAS activity.**

382 **a, b**, Electrostatic surface representation of the NCP disc surface alone (**a**) or with cGAS
383 (pink ribbon) (**b**)[30], electrostatic potential shown from red (-7) to blue (7) k·T/e. **c**, Magnified
384 view of contacts between cGAS and acidic patch of the nucleosome. **d**, Differential nuclear
385 salt fractions probed for cGAS and H2B by immunoblot from HeLa cGAS KO cells
386 reconstituted with doxycycline-inducible WT cGAS or cGAS mutants after 2 days of
387 doxycycline treatment. The experiments in **d** were independently repeated at least three
388 times with similar results. **e**, HeLa cGAS KO cells were transfected with WT cGAS-GFP or
389 mutant cGAS-GFP and the immobile fraction of nuclear localized cGAS was assessed by
390 FRAP. Data are mean ± s.d. of $n = 3$ (left) and $n = 4$ (right) independent experiments. One-
391 way ANOVA with post hoc Dunnett multiple comparison test (left) or two-tailed student's t
392 test (right). **f**, cGAMP production from HeLa cGAS KO cells reconstituted with doxycycline-
393 inducible WT cGAS or cGAS mutants after two days of doxycycline treatment. Data are
394 mean ± s.d. of $n = 4$ (left) and $n = 5$ (right) independent experiments. One-way ANOVA with
395 post hoc Dunnett multiple comparison test (left) or two-tailed student's t test (right). **g**, HeLa
396 cGAS KO cells reconstituted with doxycycline-inducible WT cGAS or cGAS mutants and
397 treated with doxycycline for 24h were co-cultured with BJ fibroblasts for 24 h. Cells were
398 lysed and mRNA levels of *IFI44* and *IFIT2* were assessed as indicated. Data are presented
399 as fold induction relative to cells without doxycycline and shown are mean values ± s.d. of n
400 = 4 independent experiments. Two-way ANOVA with post hoc Tukey multiple comparison
401 test; ns, not significant. Individual data points are from biological replicates. For gel source
402 data, see Supplementary Figure 1.

403

404

405

406 METHODS

407 **Cell culture and generation of modified cell lines.** Cells were maintained in Dulbecco's
408 modified Eagle medium (DMEM) (Life Technologies) containing 10% (v/v) fetal calf serum
409 (FCS), 1% (v/v) penicillin (10'000 IU)/streptomycin (10 mg) (BioConcept), 4.5 g/l D-glucose
410 and 2 mM L-glutamine. HeLa cells are from SIGMA (93021013-1VL) and grown under 5%
411 CO₂ and 20% O₂. Foreskin fibroblasts (BJ-5ta) were purchased from ATCC (CRL-4001) and
412 cultured at 5% O₂. cGAS KO HeLa cells were generated according to the CRISPR Cas9
413 technology as described previously [34]. The sgRNA sequences ((5'-3') fwd: CAC CGA GAC
414 TCG GTG GGA TCC ATC G; (5'-3') rev: AAA CCG ATG GAT CCC ACC GAG TCT C) were
415 cloned into the plasmid pSpCas9(BB)-2A-GFP (PX458) (AddGene, 52961). 1 µg of plasmid
416 was transfected into HeLa cells with Lipofectamine 2000 (Life Technologies). Single cells
417 were plated into wells of a 96-MW plate. Single cells were selected for GFP expression and
418 expanded to get clones, which were tested for the knockout phenotype by sequencing and
419 immunoblotting. Clones without cGAS were functionally validated. Lentiviral vectors were
420 produced as described previously [35]. Briefly, HEK 293T cells were transfected with
421 pCMVDR8.74, pMD2.G plasmids and the puromycin selectable lentiviral vector pTRIPZ
422 containing the open reading frame of the protein of interest by the calcium phosphate
423 precipitation method. The supernatant containing lentiviral particles was harvested at 48 and
424 72 h, pooled and concentrated by ultracentrifugation.

425

426 **Mutagenesis PCR.** Point mutants of human cGAS (aa155-522) were generated by site
427 directed PCR mutagenesis based on the QuickChange Primer Design method (Agilent)
428 using PrimeSTAR Max DNA Polymerase (Takara) and suitable primers. Each mutated gene
429 was cloned into a pTRIPZ vector for lentivirus production, a pET28 vector for expression of a
430 C-terminal 6 × His-Halo fusion protein in *E. coli* and a pIRESneo3 vector for FRAP
431 experiments.

432

433 **Fractionation of cellular nuclei.** 800'000 BJ-5ta fibroblasts were seeded into 10 cm culture
434 dishes. After two days cells were treated with doxorubicin (Sigma, D1515) or aclarubicin
435 (Focus Biomolecules; FBM-10-1099) as indicated and differential salt fractionations were
436 obtained as follows: Cells were lysed in a lysis buffer containing 10 mM HEPES (pH 7.4), 10
437 mM KCl, 0.5% NP40 with protease inhibitors (cOmplete™, Mini, EDTA-free Protease
438 Inhibitor Cocktail, 11836170001, SIGMA). Lysates were cleared by centrifugation and
439 supernatant A was recovered. Pellet was resuspended in a lysis buffer containing 20 mM
440 HEPES (pH 7.4) and 0.25 M NaCl. Supernatant B was recovered after centrifugation. The
441 same procedure was repeated as described above with lysis buffers containing increasing
442 NaCl concentrations (0.5 M, 0.75 M and 1 M NaCl).

443

444 **Proximity-ligation assay.** The Duolink In Situ Detection Reagents Red Kit (Sigma,
445 DUO94001, DUO92002 and DUO 92004) was used for the proximity ligation using the
446 following antibodies: Histone H2B (1:150, ab52484), Histone H4 (1:150, ab31830) (both
447 Abcam) and cGAS (1:150, D1D3G; 15102, Cell Signaling). Cells were seeded onto
448 coverslips (12 mm, Roth) at 40'000 cells per coverslip, fixed with 100% (v/v) methanol for 3
449 min and blocked with 5% BSA in PBS for 1h at room temperature. Cells were incubated with
450 the primary antibody in PBS containing 5% (w/v) BSA for 16h at 4°C in a humid chamber.
451 After washing with 1x Buffer A (Sigma), cells were processed for the proximity ligation
452 assay. Briefly, cells were incubated in anti-mouse IgG Duolink In Situ PLA Probe MINUS
453 (1:5, Sigma) and anti-rabbit IgG Duolink In Situ PLA Probe PLUS (1:5, Sigma) for 1h at
454 37°C. Thereafter, cells were washed with Buffer A and incubated in 1x Duolink Ligation
455 buffer containing DNA ligase (1:40, Sigma) for 30 min at 37°C. After incubation, cells were
456 washed in Buffer A and incubated in 1x Amplification Buffer (Sigma) with DNA polymerase
457 (1:80, Sigma) for 100 min at 37°C. Cells were washed in Buffer A and incubated for 30min at
458 37°C in 1x Detection Solution Red (Sigma). Cells were then washed in Buffer B (Sigma).
459 Cells were mounted with the medium Duolink In Situ Mounting Medium with DAPI (Sigma).
460 Images were acquired using a 63x/1.4 oil objective on a confocal laser scanning microscope
461 (Zeiss LSM700). Confocal imaging was performed with Z-sections for at least 10 randomly
462 chosen fields. Maximum intensity projection was applied on the images. The number of PLA
463 positive signal per cell within the DAPI positive area was counted using the Cell Counter
464 plugin in Fiji.

465

466 **cGAMP measurement.** HeLa cells reconstituted with WT cGAS or cGAS mutants were
467 plated (0.075 x10⁶ cells/ ml) in the presence of doxycycline (0.1 – 1 µg/ml) for 2 days. Cells
468 were harvested by trypsination (Trypsin-EDTA (0.05%), Life Technologies) for 5 min. Cell
469 pellets were lysed in RIPA lysis buffer containing 50 mM Tris, 150 mM NaCl, 1% (w/v)
470 sodium deoxycholate, 0.03% (v/v) SDS, 0.005% (v/v) Triton X-100, 5 mM EDTA, 2 mM
471 sodium orthovanadate and cOmpleteTM Protease Inhibitor Cocktail (Roche) (pellet from one
472 well of a 6-well-plate in 130 µl of RIPA) for 30 min on ice. Lysed cells were centrifuged for 5
473 min at 18,200 g and 4°C. Diluted supernatants were used for cGAMP ELISA assay (Cayman
474 2'-3'-cGAMP ELISA kit - 501700) according to the manufacturer's instructions. Protein
475 concentration in the supernatant was measured using BCA Pierce Protein assay kit and was
476 used to normalize cGAMP concentration.

477 **Immunoblotting.** Protein extracts were loaded into 10% or 15 % SDS-polyacrylamide gels.
478 cGAS was blotted onto nitrocellulose membrane (0.45 µm, BioRad) and histones were
479 transferred on Polyvinylidene difluoride membrane (0.2 µm, BioRad). The primary antibody

480 was incubated in 5% bovine serum albumin diluted in PBS 1x overnight at 4°C. The
481 secondary antibodies anti-mouse or anti-rabbit HRP-conjugated antibodies were incubated
482 for 1 h at room temperature. Proteins were visualized with the enhanced chemiluminescence
483 substrate ECL (Pierce, ThermoScientific) and imaged using the ChemiDox XRS Biorad
484 Imager. The following antibodies were used in this study: Histone H2B (1:1000, ab52484),
485 Histone H2A (1:1000, ab18255), Histone H4 (1:1000, ab31830) (all Abcam); cGAS (1:1000,
486 D1D3G; 15102), Histone H3 (1:1000, 9715), STING (1:1000, D2P2F) (all Cell Signaling),
487 Lamin A/C (1:1000, SAB4200236, Sigma), GAPDH (1:1000, AM4300, LifeTechnologies),
488 donkey anti-Rabbit HRP (1:5000; 711-036-152) and donkey anti-Mouse HRP (1:5000; 715-
489 036-151) (both Jackson ImmunoResearch).

490

491 **Confocal imaging of endogenous cGAS and H2B.** 40'000 cells were seeded on
492 coverslips (12 mm, Roth). At 48h after seeding, cells were fixed with 100% (v/v) methanol for
493 3 min and blocked with PBS containing 5% (w/v) BSA for 1h at room temperature.
494 Cells were incubated with the primary antibodies (1:150, rabbit anti-cGAS (15102S, CST)
495 and mouse anti-H2B (1:150; ab52484, abcam) in PBS containing 5% (w/v) BSA for 16h at
496 4°C in a humid chamber. Afterwards, coverslips were washed with PBS three times and then
497 incubated in PBS containing 5 µg/ml of 4',6-diamidino-2-phenylindole (DAPI) and the
498 secondary antibodies (1:1000; goat anti-rabbit IgG (H+L) Alexa Fluor 488 conjugate
499 (A11008, Thermo) and donkey anti-mouse IgG (H+L) Alexa Fluoro 568 conjugate (A10037,
500 Thermo)). At 1h post-incubation coverslips were washed three times with PBS 1X and
501 mounted on microscope slides (15545650, Thermo) using Fluoromount-G (0100-01,
502 SouthernBiotech). Images were acquired using a 63x/1.40 HC Plan-Apochromat oil
503 immersion objective on a SP8-STED 3X confocal microscope (Leica). cGAS labelled with
504 Alexa Fluor 488 was imaged with an excitation laser of 488 nm and emission window of 492-
505 532 nm, detected with a hybrid detector. Nuclei counterstained with DAPI were imaged with
506 an excitation laser of 405 nm and emission window of 410-480 nm, detected by a
507 photomultiplier detector. H2B was labelled with Alexa Fluor 568 and imaged with an
508 excitation laser of 561 nm and emission window of 560-620 nm, detected by a hybrid
509 detector. Images were acquired with a voxel size of 0.0655x0.0655x1 µm³.

510

511

512 **Fluorescence recovery after photobleaching.** HeLa cGAS-KO cells were plated on 35
513 mm glass bottom culture dishes (MatTek Corporation – Part Number P35G-1.5-14-C) at
514 5,000 cells per dish. On the next day, cells were transfected with plasmids encoding for
515 hcGAS-GFP WT or cGAS mutants (pIRESneo3 hs cGas GFP, pIRESneo3 hs cGAS K350A
516 L354A GFP, pIRESneo3 hs cGAS R236A GFP, and pIRESneo3 hs cGAS R255A GFP)

517 using Lipofectamin 2000 following the manufacturer instructions. After 24 h cells were used
518 for FRAP experiments, which were performed on a ZEISS LSM 710 confocal microscope at
519 37°C with a W-Plan Apochromat 63x/1.0 objective. A circle of 1.33 μm diameter (10 pixels)
520 within hcGAS-GFP signal located inside nucleus was partially photobleached with 488-nm
521 laser (100% power) with 20 iterations within 0.200 seconds. Time-lapse images were
522 acquired over a 20-second time course after photobleaching with 0.200 second intervals
523 with a laser power between 0.4 and 0.6 %. Images were processed by Fiji and normalized
524 on FRAP Analyser (Software developed at the University of Luxembourg) using the Single
525 Normalization+Full scale method. FRAP data were fitted to a binding+diffusion circular
526 model using the FRAP Analyser. Immobile fraction extracted data were plotted in GraphPad
527 Prism 8.

528

529 **Fluorescence polarization (FP).** FIC-labelled 21 bp dsDNA oligonucleotide (5'-FIC-
530 GACCTTTGTTATGCAACCTAA-3') was used as a fluorescent tracer. Increasing amounts of
531 WT or K394E cGAS (0.3-2500 nM) were mixed with tracer (10 nM final concentration) in a
532 384-well microplate (Greiner, 784076) at room temperature. The interaction was measured
533 in a buffer containing 20 mM HEPES pH 7.4, 500 μM TCEP, 40 mM NaCl, 10 mM KCl, 0.1%
534 (v/v) pluronic acid. PHERAstar FS microplate reader (BMG Labtech) equipped with a
535 fluorescence polarization filter unit was used to determine the changes in fluorescence
536 polarization. The polarization units were converted to fraction bound as described previously
537 [36]. The fraction bound was plotted versus cGAS concentration and fitted assuming a 1:1
538 binding model to determine the dissociation constant (K_d) using Prism 7 (GraphPad). Since
539 the oligonucleotide that was used contained a fluorescent label, we refer to these as
540 apparent K_d (K_{app}). All measurements were performed in triplicates. For the competitive
541 titration assays, the cGAS bound to the fluorescent oligo tracer was back-titrated with
542 unlabeled dsDNA (21, 147, 167, 227 bp) or mono-nucleosomes (146, 167, 227 bp). These
543 counter-titration experiments were carried out by mixing tracer (10 nM) and cGAS (300 nM),
544 and titrating increasing concentration of the unlabeled competitor (0 – 2.5 μM). The fraction
545 bound was plotted versus competitor concentration and the data were fitted with a nonlinear
546 regression curve to obtain the IC_{50} values in Prism 7 (GraphPad). At least two technical
547 replicates were performed per experiment.

548

549 **Cellular activation assays.** HeLa cells reconstituted with WT cGAS or cGAS mutants were
550 seeded (0.075×10^6 cells/ml) in 6-well plates in the presence of doxycycline (1 $\mu\text{g}/\text{ml}$) for 16h
551 or 40h. Stimulation with dsDNA (90bp) was carried out as previously described [35]. Briefly,
552 dsDNA (1.6 $\mu\text{g}/\text{ml}$) was transfected using Lipofectamine 2000 (Life Technologies) and cells

553 were harvested 4h later. For co-culture studies, HeLa cells were treated with doxycycline as
554 described above. After 24h cells were collected, washed, and 19.000 cells were mixed with
555 human BJ fibroblasts (0.095×10^6 cells/ml), and incubated overnight.

556

557 **Quantitative real-time PCR.** Cells were lysed using RLT buffer (Qiagen - 79216). RNA was
558 extracted according to the manufacturer's protocol (Qiagen RNeasy Mini kit) and treated
559 with RNase-free DNase (Thermo Scientific - EN0521). 500 ng of RNA was reverse
560 transcribed (RevertAid, Thermo Fisher Scientific - EP0442) and analyzed by RT-qPCR in
561 duplicates or triplicates using the Maxima SYBR Green/ROX qPCR Master Mix (Thermo
562 Fisher Scientific - K0223). The qPCR reactions were run on a QuantStudio 5 Real-Time
563 PCR system. GAPDH was used for normalization. Primer sequences (5'-3'): *GAPDH*: fwd
564 GAGTCAACGGATTTGGTCGT, rev GACAAGCTTCCCGTTCTCAG; *IFI44*: fwd GAT GTG
565 AGC CTG TGA GGT CC, rev CTT TAC AGG GTC CAG CTC CC; *IFIT2*: fwd
566 GCGTGAAGAAGGTGAAGAGG, rev GCAGGTAGGCATTGTTTGGT; *cGAS*: fwd
567 GCACGTGAAGATTTCTGCACC, rev TGA CTCAGAGGATTTTCTTTTCGG. The sequence of
568 the sense strand of the 90-mer DNA is as follows (5'-3'): TACAGAT
569 CTACTAGTGATCTATGACTGATCTGTACATGATCTACATACAGATCTACTAGTGATCTAT
570 GACTGATCTGTACATGATCTACA.

571

572 **Expression and purification of recombinant cGAS.** Truncated human cGAS (155-522)
573 WT or mutants were expressed and purified from *Escherichia coli* strain BL21 (DE3).
574 Plasmids expressing His6-Halo tagged truncated human cGAS were induced with 2 mM
575 IPTG at 18°C for 20 h. Bacteria were collected by centrifugation and lysed by sonication in
576 lysis buffer (20 mM HEPES, pH 8.0, 300 mM NaCl, 20 mM imidazole, 1 mM DTT, and
577 protease inhibitor). After centrifugation, clear lysate was incubated with Ni-NTA beads
578 (Qiagen), washed with lysis buffer and 20 mM HEPES, pH 8.0, 1 M NaCl, 20 mM imidazole,
579 1 mM DTT and eluted with 20 mM HEPES, pH 7.5, 500 mM NaCl, and 250 mM imidazole.
580 Eluted cGAS was subjected to size-exclusion chromatography using a Superdex 200 16/60
581 column in 20 mM HEPES pH 7.5, 300 mM KCl, 1 mM DTT. The protein was flash frozen in
582 liquid nitrogen and stored at -80°C.

583

584 **Electrophoretic mobility shift assays.** For the cGAS mutants, biotinylated
585 mononucleosomes (Active motifs, 31583) were incubated with serial dilutions of recombinant
586 cGAS at room temperature for 30 min in PBS for sample volume of 10 μ l. The binding
587 reactions contained mononucleosomes 40 μ g/ml and cGAS proteins ranged from 100 μ g/ml
588 to 12 μ g/ml with 2-fold increase. After reaction, 5 μ l glycerol was added. Reactions were
589 detected by electrophoresis on a 5% PAGE gel in 0.5 \times TBE buffer at 10mA for 1h15. The

590 gels were incubated 15min in SyBrSafe containing PBS and were scanned using the
591 Typhoon FLA-9500 imager (GE healthcare) and imaged using the ChemiDoc XRS Biorad
592 Imager and Image Lab 6.0.0 software. For the EMSA assay using the LANA peptide,
593 biotinylated mononucleosomes (Active motifs, 31583, 40 µg/ml) were incubated with the
594 LANA from 0.6 mg/ml to 78 µg/ml, two-fold dilutions at room temperature for 5 min in PBS
595 for sample volume of 4 µL. 40 pmol recombinant cGAS WT in 4µl PBS was added and
596 incubated 30min at RT. After reaction, 5 µl glycerol was added. Reactions were detected by
597 electrophoresis on a 5% PAGE gel in 0.5× TBE buffer at 10mA for 1h15. The gels were
598 incubated 15min in SyBrSafe containing PBS and were scanned using the ChemiDoc XRS
599 Biorad Imager and Image Lab 6.0.0 software (Biorad).

600

601 **cGAS *in vitro* competition assay.** 50 nM human cGAS was mixed with recombinant
602 histones and H2A/H2B dimer (5 to 0.3 µM) or mononucleosomes (75nM to 2nM) or
603 nucleosome fibers (6.5nM to 0.1nM) in HEPES 10 mM pH 8.0, KCl 10 mM MgCl₂ 1mM. 0.1
604 mg/ml HT-DNA, 10 µCi [α -³²P]ATP and 1 mM GTP were added and left to react for 12 h at
605 37°C. Reaction solution (1 µl) was spotted onto TLC plates (HPTLC silica gel, 60 Å pores,
606 F₂₅₄, 1055480001; MERCK Millipore), and the nucleotides were separated with 5 mM NH₄Cl
607 15%/85% EtOH as the mobile phase at 25°C for 30 min. The plates were visualized by
608 autoradiography and scanned using the Typhoon FLA-9500 Imager (ImageQuanTool, GE
609 Healthcare). Images were processed using Image Lab 6.0.0 software (Biorad) to quantify the
610 intensity of the spots corresponding to cGAMP. After normalizing by cGAMP levels in
611 absence of chromatin for each individual mutant, IC50 was calculated using GraphPad
612 Prism.

613

614 **Large scale production of 601 DNA.** Production of 601 DNA was performed as previously
615 described [37]. Briefly, a plasmid carrying 32 copies of the Widom “601” sequence, each
616 flanked by EcoRV restriction sites, was purified from an 8L 2YT culture of transformed *E. coli*
617 DH5α cells using alkaline lysis, followed by isopropanol-precipitation, RNase A treatment of
618 the suspended pellet and subsequent chromatography on Sepharose 6. After isopropanol
619 precipitation, the 601 sequences were released from the plasmid by digestion with EcoRV
620 (12 ml total volume containing 132 µl EcoRV for 40 h). The 601 DNA fragment was isolated
621 by incremental PEG-precipitation with 14.5 % PEG, and further purified by ethanol-acetate
622 precipitation and subsequent chloroform-phenol extraction to yield 9.2 mg of “601” DNA.

623

624 **Mononucleosome preparation.** Histones were prepared and octamers made as described
625 [38]. Mono-nucleosomes were reconstituted through overnight gradual dialysis from
626 TEK2000 (10 mM Tris pH 7.5, 1 mM EDTA, 2 M KCl) into TEK10 (10 mM Tris pH 7.5, 1 mM

627 EDTA, 10mM KCl) with dialysis buttons using octamer/DNA ratios of 1.3, 1.4 and 1.5 each in
628 0.9 ml total volume containing 6.7 μ M DNA. After recovering the material from the dialysis
629 buttons, the mono-nucleosomes were concentrated using Amicon centrifugal concentrators
630 with a 30 kDa MWCO to yield a nucleosome concentration of 0.86 mg/ml.

631

632 **Cryo-EM sample preparation.** 147bp-601Widom-sequence-NCPs and purified human
633 cGAS were mixed in a 1:1.5 molar ratio in gel filtration buffer (20 mM HEPES pH 7.4, 300
634 mM KCl and 250 μ M TCEP) and dialyzed for 24h against low salt dialysis buffer (20 mM
635 HEPES pH 7.4, 50 mM KCl and 250 μ M TCEP). Thereafter the dialyzed complex was
636 concentrated using Amicon Ultra-0.5mL centrifugal filter (Merck Millipore) and applied to
637 GraFix [15] gradient of 10-30 % sucrose containing top solution (20 mM HEPES pH 7.4, 50
638 mM KCl and 250 μ M TCEP, 10% w/v sucrose) and bottom solution (20 mM HEPES pH 7.4,
639 50 mM KCl and 250 μ M TCEP, 30% w/v sucrose, 1.5% glutaraldehyde). The gradient
640 ultracentrifugation was carried at 30000 rpm, 18 h, 0°C using AH-650 swinging bucket rotor.
641 100 μ L fractions were collected and analysed by both native PAGE and SDS-PAGE.
642 Thereafter the peak fractions were combined and dialyzed overnight (20 mM HEPES pH 7.4,
643 50 mM KCl and 250 μ M TCEP) to remove sucrose. The resulting complex sample was
644 concentrated with Amicon-Ultra 0.5mL centrifugal filter to 1 mg/ml as determined by
645 measuring protein concentration at Abs280. Quantifoil holey carbon grids (R 1.2/1.3 200-
646 mesh, Quantifoil Micro Tools) were glow discharged with Solarus plasma cleaner (Gatan) for
647 30 sec in a H₂O₂ environment. 3 μ L of sample was applied to grids and were blotted for 3 s
648 at 4°C at 100% humidity in a Vitrobot Mark IV (FEI, Hillsboro, OR, USA), and then
649 immediately plunged into liquid ethane.

650

651 **Cryo-EM data acquisition.** 1. cGAS(K394E)-NCP complex: Two data sets for the
652 cGAS(K394E)- NCP complex were collected for GraFix crosslinked samples using Titan
653 Krios (Thermo Fisher Scientific) electron microscope at 300 keV. Zero-energy-loss (slit 20
654 eV). Automatic data collection was done using EPU (Thermo Fisher Scientific) on a Cs-
655 corrected (CEOS GmbH, Heidelberg, Germany) with micrographs recorded using a Gatan
656 K2 summit direct electron detector (Gatan). The acquisition was performed at a nominal
657 magnification of 130,000 \times in EFTEM nanoprobe mode yielding a pixel size of 0.86 Å at the
658 specimen level. All datasets were recorded with the 100 μ m objective aperture and with total
659 dose of 45 e-/Å² recording 40 frames. The targeted defocus values ranged from -0.5 to -2
660 μ m. Similarly, few micrographs were recorded for the two non-crosslinked samples, wild type
661 cGAS-NCP complex and dimerisation mutant (K394E) cGAS-NCP complex.

662 2. cGAS(WT)-NCP complex: A data set for the cGAS(WT)-NCP complex was collected
663 for GraFix crosslinked samples using Glacios (Thermo Fisher Scientific) electron microscope
664 at 200 keV. Automatic data collection was done using EPU (Thermo Fisher Scientific) on a
665 Cs-corrected (CEOS GmbH, Heidelberg, Germany) with micrographs recorded using a
666 Falcon 3EC Direct Electron Detector. The acquisition was performed at a nominal
667 magnification of $150,000\times$ in EFTEM nanoprobe mode yielding a pixel size of 0.68 \AA at the
668 specimen level. All datasets were recorded with the $100\text{ }\mu\text{m}$ objective aperture and with total
669 dose of $35\text{ e}/\text{\AA}^2$ recording 40 frames. The targeted defocus values ranged from -0.5 to -2
670 μm .

671

672 **Cryo-EM image processing.** 1. cGAS(K394E)-NCP complex: On-the-fly evaluation of the
673 data was performed with CryoFLARE (in house development; www.cryoflare.org)
674 (<https://doi.org/10.1101/861740>). Micrographs below EPA limit of 5 \AA were used for further
675 processing. A total of 2890 micrographs were acquired in two sessions. Drift correction was
676 performed with the Relion3 motioncor where a motion corrected sum of all 40 frames was
677 generated with and without applying a dose weighting scheme and CTF was fitted using
678 gCTF [39] on the non-dose-weighted sums. A small set of particles (54000) were picked
679 were picked using crYOLO [40] and imported to cryoSPARC [32]. After 2D classification, an
680 *ab initio* model was generated. This model was used as initial 3D map for further 3D
681 classification in Relion 3 for the two datasets independently. In dataset 1, the particles
682 (13943) included in the class containing two cGAS and two NCPs were imported in
683 cryoSPARC [32] and subjected to non-uniform refinement and later refined to 4.1 \AA
684 (**Extended Data Table 1a**). In dataset 2, the particles (87323) included in the class
685 containing one cGAS and one NCP were subjected to local refinement in cryoSPARC and
686 refined to 3.8 \AA . The particles used for the 4.1 and 3.8 \AA maps were merged and refined to
687 3.3 \AA in Relion 3 [41]. CTF refinement and signal subtraction was done for the density
688 accounting for 1cGAS-1NCP complex. 3D classification followed by non-uniform refinement
689 in cryoSPARC led to a 3.1 \AA map.

690 2. cGAS(WT)-NCP complex: A total of 5007 movies were acquired for the cGAS(WT)-NCP
691 complex. Full frame motion correction followed by patch CTF was performed using
692 cryoSPARC. Particle picking was done using template picker for seven hundred images and
693 2D template generated. Selected 2Ds were later used to generate a *ab-initio* model and
694 template picking of particles for rest of the images in cryoSPARC. A total of 142743
695 particles out of 404087 were selected from 2D classification to do a homo refinement. 3D
696 hetero refinement with two classes was carried out with 56747 (40%) particles giving a map
697 which later was locally refined to 5.1 \AA . Same class with 56747 particles was further used for

698 particle subtraction for NCP1- cGAS1 complex and further local refinement was carried out
699 to obtain a 4.7 Å map.

700 The resolution values reported for all reconstructions are based on the gold-standard Fourier
701 shell correlation curve (FSC) [31]. High-resolution noise substitution has been used for
702 correcting the effects of soft masking for the related FSC curves. All the maps have been
703 filtered based on local resolution estimated with MonoRes (XMIPP) [42] and later sharpened
704 using the *localdeblur_sharpen* protocol (XMIPP).

705

706 **Model building and refinement.** A nucleosome model from PDB entry 6R8Y [43] and a
707 human cGAS model from PDB entry 4LEV [16] were used as initial references for the cryo-
708 EM map interpretation. The models were rigid-body docked using Chimera [44] and COOT
709 [45]. Sequence reassignment to 6R8Y with the 147 bp 601 Widom sequence [46] along with
710 the human histone sequence was done. The starting model for cGAS (4LEV) was refined
711 against the corresponding crystallographic structure factors with Phenix [47] and Rosetta
712 [48] to resolve some of the geometry outliers. Restraints for the covalently attached
713 crosslinker were generated with JLigand [49], Phenix, and Rosetta. Model building and
714 refinement of the cryo-EM structures were carried out iteratively with COOT [45], Phenix
715 [47], and Rosetta [48] using reference model restraints for cGAS (torsional angles) derived
716 from the template model (see above). The reference model restrains were generated with
717 Phenix [47], and converted to Rosetta constraints. Residues at the interface with the NCP
718 were not restrained. In case of the dimeric nucleosome-cGAS the refinement was with
719 reference model restraints derived from the higher resolution monomer complex (torsional
720 angles). Model validation was done with Phenix [47] and MOLPROBITY [50]. Sidechains
721 without sufficient density were marked with zero occupancy.

722

723

724

725

726

727 **Extended Data Figure Legends**

728

729 **Extended Data Fig. 1 | H2A-H2B dimers bind and inhibit cGAS.**

730 **a**, Confocal microscopy images of human BJ fibroblasts stained with primary antibodies
731 against cGAS (green) and H2B (red). DNA was stained with DAPI (blue). Scale bar, 25 µm.

732 **b**, Human BJ fibroblasts were treated with aclarubicin (20 µM) as indicated. Differential
733 nuclear salt fractions were obtained, and the presence of the indicated proteins within each
734 fraction was monitored by immunoblot. In **a** and **b**, the experiments were independently

735 repeated at least three times. **c**, Human BJ fibroblasts were treated with DMSO (control) or
736 aclarubicin (20 μ M) for 2 h. After fixation, cells were subjected to PLA with anti-cGAS, anti-
737 H2B, and anti-H4, respectively. PLA signals were quantified from at least 50 individual cells.
738 Representative images are displayed (left) and data (right) are mean \pm s.d. of one
739 representative experiment out of $n = 3$ independent experiments. Two-tailed student's t -test.
740 Scale bar, 20 μ m. **d**, Specificity control for PLA with human BJ fibroblasts using single
741 antibody staining for cGAS, H2B, and H4, respectively. Scale bar, 20 μ m. The experiment
742 was repeated three times with similar results. **e**, Relative levels of *in vitro* cGAMP synthesis
743 in the presence or absence of a concentration gradient of mononucleosomes (from 75 nM to
744 1 nM) and chromatin fibers (from 6 nM to 0.1 nM). **f**, **g**, Relative levels of *in vitro* cGAMP
745 synthesis in the presence or absence of a concentration gradient of histone H2A, H2B or
746 H2A-H2B dimers (from 5 μ M to 0.3125 μ M; 1:2 step dilutions) (**f**) or H3 and H4 (from 5 μ M to
747 0.3125 μ M) (**g**). cGAS (catalytic domain; aa 155-522; hcGAS) activation was induced by HT
748 DNA and data are mean \pm s.d. of $n = 3$ independent experiments. One-way ANOVA with
749 post hoc Dunnett multiple comparison test (**e-g**). **h**, Calculated IC_{50} values without (IC_{50}) or
750 with (cor. IC_{50}) correction for the number of cGAS binding sites per molecule
751 (mononucleosome or fiber). Data points are from experimentally independent experiments.
752 For gel source data, see Supplementary Figure 1.

753

754 **Extended Data Fig. 2 | Cryo-EM analysis of cGAS bound to nucleosomes.**

755 **a**, Cryo-EM micrograph of the non-crosslinked sample containing wild-type cGAS(WT)
756 bound to NCP. Scale bar, 20 nm (Micrograph is representative of 20 images taken). **b**, Cryo-
757 EM micrograph of the non-crosslinked sample containing dimerisation mutant cGAS(K392E)
758 bound to NCP. Scale bar, 20 nm (Micrograph is representative of 20 images taken). The
759 cGAS-NCP complexes were directly concentrated and frozen on grids after gel filtration
760 chromatography. Chromatin fibers induced by cGAS binding are highlighted by white
761 rectangles (**a**, **b**). **c** and **d**, Magnified view of oligomeric assemblies extracted from **a** and **b**
762 (starred rectangles), respectively.

763

764 **Extended Data Fig. 3 | Schematics of cGAS-NCP structure determination,** 765 **classification and refinements.**

766 **a**, Representative denoised cryo-EM micrograph of cGAS-NCP complex derived using
767 JANNI ($n = 2,890$ micrographs). Scale bar, 20 nm. **b**, Reference-free 2D class averages of
768 the particles picked using crYOLO. **c**, Data processing scheme starting with an *ab initio*
769 model derived from 2D classes (**b**) for 34,000 particles. The scheme is divided into two
770 separate datasets. On the right, data processing for in the a 4.1 \AA dimeric structure of

771 2NCP-2cGAS. 103,688 particles were subjected to 3D classification using *RELION 3.0* [31]
772 leading to four classes. The best class containing dimeric particles with 2NCP-2cGAS was
773 further subjected to a second round of 3D classification producing two classes. The class
774 containing 13,943 dimeric particles was further polished, 3D refined using *RELION 3.0* and
775 later CTF refined using cryoSPARC [32], generating a 4.1 Å map. The left side of the
776 scheme shows the data processing for the 3.1 Å structure of 1NCP-1cGAS. 289,518
777 particles were subjected to 3D classification using *RELION 3.0* [31] resulting in four classes.
778 The best class containing 87,323 dimeric particles with 2NCP-2cGAS was further polished
779 and merged with the 13,943 particles used for 4.1 Å map. The merged particles were
780 subjected to CTF refinement and signal subtraction for the density accounting for 1cGAS-
781 1NCP. 3D classification followed by non-uniform refinement in cryoSPARC led to a 3.1 Å
782 map. **d**, Gold-standard Fourier shell correlation curves are shown for the 3.1 Å monomer
783 map (blue) and the 4.1 Å dimer map (orange). **e** and **f**, local resolution filtered maps
784 (MonoRes) for the 4.1 Å dimer map and 3.1 Å monomer map, respectively. **g** and **h**, angular
785 distribution plots shown for the 3.1 Å monomer map and 4.1 Å dimer map respectively.

786

787 **Extended Data Fig. 4 | Cryo-EM structure of wild-type cGAS bound to nucleosomes.**

788 **a**, A 5.1 Å 3D reconstruction of the complex containing two wild-type cGAS protomers,
789 cGAS₁ (red) and cGAS₂ (orange), and two nucleosomal core particles, NCP₁ and NCP₂,
790 respectively. **b**, Ribbon diagram of the dimerisation mutant (K394E) NCP₁-cGAS₁-cGAS₂-
791 NCP₂ model rigid-body fit into wild type NCP₁-cGAS₁-cGAS₂-NCP₂ electron-density maps. **c**,
792 3D focused classification map of NCP₁-cGAS₁ shown at low contour levels. **d**, Magnified
793 view of cGAS₁ and NCP₁ DNA interactions. The zinc ion (cyan sphere) is coordinated by
794 residues H390, C396, C397 and C404 forming the zinc finger motif. Residue K394 (sapphire
795 blue sphere), is part of loop coordinating the zinc ion and is positioned close to the DNA of
796 NCP₁. Electron density connecting the NCP₁ DNA and the cGAS₁ zinc ion coordinating loop
797 is shown in the background. **e**, A 4.1 Å EM map of the dimerisation mutant cGAS(K394E)-
798 NCP complex. **f**, A 5.1 Å EM map of the wild-type cGAS-NCP complex. **g**, EM maps from
799 the mutant cGAS-NCP complex (grey)(**e**) superposed onto the wild-type cGAS-NCP
800 complex map (blue) (**f**). The map-to-map fit gives a correlation value of 0.87 (Extended Data
801 Table 1b).

802

803 **Extended Data Fig. 5 | Schematics of wild-type cGAS-NCP structure determination,**
804 **classification and refinements.**

805 **a**, Representative denoised cryo-EM micrograph of cGAS-NCP complex derived using
806 JANNI (n= 5,007 micrographs). Scale bar, 25 nm. **b**, Reference-free 2D class averages of
807 the particles picked using crYOLO. **c**, Data processing scheme starting with an *ab initio*

808 model derived from 2Ds (**b**) is shown using 16,000 particles. The scheme is divided into two
 809 sub-schemes. The left side shows the processing of data for a 5.1 Å dimeric structure of
 810 NCP₁-WTcGAS₁-WTcGAS₂-NCP₂. 142,743 particles were subjected to 3D hetero refinement
 811 classification using cryoSPARC leading to two classes. The best class containing dimeric
 812 particles with WTcGAS₂-NCP₂ was further subjected to local refinement and later CTF
 813 refined using cryoSPARC generating a 5.1 Å map. For the scheme on the right, 56,747
 814 particles were subjected to particle subtraction. The class containing 56,747 dimeric
 815 particles with WTcGAS₁-NCP₁ was locally refined and later CTF refined using cryoSPARC
 816 generating a 4.7 Å map. **d**, Gold-standard Fourier shell correlation curves are shown for the
 817 reconstructions, 5.1 Å (blue) and 4.7 Å (red). **e**, Local resolution filtered maps (MonoRes) for
 818 the 5.1 Å dimer map. **f**, Local resolution filtered maps (MonoRes) for the 4.7 Å monomer
 819 map. **g**, Angular distribution for the dimer 5.1 Å map. **h**, Angular distribution for the 4.7 Å
 820 monomer map.

821

822 **Extended Data Fig. 6 | Interaction of cGAS₁ with NCP₁ and mechanism of inhibition.**

823 **a**, Ribbon diagram and a 3D reconstruction of the complex containing cGAS1 (red) and
 824 NCP1 (gray, blue). **b-f**, EM densities (shown as mesh at 4.5σ) for the residues interacting
 825 with the nucleosome in *cis*. Shown are cGAS Loop1, Loop2 and Loop3 interactions in *cis*
 826 with H2A-H2B dimer respectively (**b-d**) and the interactions of cGAS helix α5 residues with
 827 the DNA backbone from NCP1 (**e, f**). **g**, Overview of the hcGAS-DNA 2:2 minimal cGAS-
 828 DNA active dimer complex to highlight the two distinct DNA-binding surfaces (A-site and B-
 829 site) as previously defined [16] (PDB: 4LEY). **h**, Superposition of the hcGAS-DNA complex
 830 (**g**) onto the cGAS-NCP complex as defined in this work (Fig. 2g). **i**, Magnified view of the
 831 common binding site (B-site) showing the clash of the two DNA strands with the
 832 nucleosomal DNA (orange, ligand DNA and gray, nucleosomal DNA).

833

834 **Extended Data Fig. 7 | Interaction of cGAS with nucleosomes *in vitro*.**

835 **a**, EMSA gel showing the interaction of nucleosomes (40 ng/μl) with WT cGAS (40 pmol) in
 836 presence of increasing concentrations of LANA peptide WT or AA mutant (from 0.6 mg/ml to
 837 78 μg/ml; 1:2 step dilution). Dark grey arrowhead: nucleosomes complexed with cGAS, light
 838 grey arrowhead: free nucleosomes. Data are representative for three independent
 839 experiments. **b**, *In vitro* cGAMP synthesis of WT hcGAS (50nM) with chromatin (5 nM) in
 840 presence of a gradient concentration of LANA peptide WT or AA mutated (from 0.5mg/ml to
 841 0.125 mg/ml; 1:2 step dilution) normalized by cGAMP levels in absence of chromatin. Mean
 842 ± s.d. of *n* = 3 independent experiments is shown. One-way ANOVA with post hoc Dunnett
 843 multiple comparison test. Data points are from experimentally independent experiments. **c**,
 844 *In vitro* cGAMP synthesis of WT, R255A and R236A hcGAS (all 200nM) with a concentration

845 gradient of 147bp dsDNA or mono-nucleosome (no DNA overhang) (left) or 227bp dsDNA or
 846 mono-nucleosomes (80bp dsDNA overhang) (right) (from 200 nM to 50 nM; 1:2 step
 847 dilutions) normalized by cGAMP levels for 200nM dsDNA for each individual mutant. Mean \pm
 848 s.d. of $n = 3$ independent experiments is shown. **d**, 10 nM of a fluorescein (Fic) labelled 21
 849 bp dsDNA tracer were mixed with 300 nM cGAS protein and counter-titrated with unlabelled
 850 DNA (left) or nucleosomes (right) (see Methods). **e**, Forward titration experiments using 10
 851 nM Fic-labelled probe in the presence of increasing amounts of either WT cGAS or cGAS
 852 pre-treated with 0.1-5 mM EDTA as indicated. **f**, Forward titration as in (**a**) but with cGAS
 853 K394E, either pre-treated with 0.1 mM EDTA or not. **g**, As in (**d**) but the cGAS protein was
 854 pre-treated with EDTA as indicated. For (**d**) and (**g**), all data include two technical replicates
 855 and all data points are explicitly shown. Affinities are indicated as IC_{50} values. For (**e**) and (**f**),
 856 all data include three technical replicates and are shown as mean \pm s.d. Affinities are
 857 indicated as apparent K_d (K_{app}) values. For gel source data, see Supplementary Figure 1.

858

859 **Extended Data Fig. 8 | cGAS interactions with the second nucleosome *in trans*.**

860 **a**, EM envelope of the dimeric complex containing NCP1-cGAS1-cGAS2-NCP2. **b**, A
 861 magnified view of an additional density accounting for N-terminal tail of histone H4. **c**, A 3D
 862 class showing the additional EM density found (dotted circles) near the outward facing acidic
 863 patch. The dimeric structure of NCP1-cGAS1-cGAS2-NCP2 is modelled into the major
 864 density. **d**, Modelling of cGAS molecules on the outer sides of the two NCP molecules in the
 865 map (**c**) resulting in a complex of cGAS1'-NCP1-cGAS1-cGAS2-NCP2-cGAS2'. **e**, A
 866 representative micrograph containing a cGAS (WT)-NCP multimeric complex ($n = 20$
 867 micrographs). **f**, Magnified view on oligomeric assemblies extracted from (**e**) (left), Scale bar,
 868 10 nm, and a modelled arrangement of cGAS-NCP in cartoon representation (right). **g**,
 869 Differential nuclear salt fractions probed for cGAS and H2B by immunoblot from HeLa cGAS
 870 KO cells reconstituted with doxycycline-inducible WT cGAS or cGAS K285A/R300A/K427A
 871 after 2 days of doxycycline treatment. One representative experiment of $n = 3$ independent
 872 experiments is shown. For gel source data, see Supplementary Figure 1.

873

874 **Extended Data Fig. 9 | Effect of structure-guided mutations in cells.**

875 **a**, Lines show FRAP recovery curves obtained after photo-bleaching WT cGAS-GFP or
 876 cGAS-GFP mutants inside the nucleus of cGAS KO HeLa cells. Data show mean \pm SEM
 877 from 20-25 measurements. Graph is representative of $n = 3$ (left panel) or 4 (right panel)
 878 independent experiments. **b-d**, HeLa cGAS KO cells reconstituted with doxycycline-inducible
 879 WT cGAS or cGAS mutants were treated with doxycycline (1 μ g/ml) for 16h and 40h (**b**, **c**) or
 880 40h (**d**), respectively. In (**b**) cells were lysed and mRNA levels of *IFI44*, *IFIT2* and *CGAS*
 881 were assessed. Data are presented as fold induction relative to non-treated WT cGAS and

882 are mean \pm s.d. of $n = 5$ independent experiments. Two-way ANOVA with post hoc Tukey
 883 multiple comparison test. In (c) cells were lysed and STING and GAPDH levels were
 884 assessed by immunoblot. One representative experiment for $n = 3$ (16h) and $n = 3$ (40h)
 885 experiments with similar results is shown. In (d) cells were stimulated with dsDNA (90mer)
 886 for 4h or left untreated (Ctrl.) and mRNA levels of *IFI44* and *IFIT2* were measured. Data
 887 show as mean \pm s.d. of $n = 2$ independent experiments. Individual data points represent
 888 biological replicates. For gel source data, see Supplementary Figure 1. e, cGAS multiple
 889 sequence alignments showing the sequence conservation of residues involved in
 890 interactions with the acidic patch, nucleosome binding in *cis*, and nucleosome binding in
 891 *trans*. cGAS sequences from Human, Monkey, Bovine, Pig, Mouse and Rat corresponding
 892 to UniProt ID's Q8N884, F7B8L6, E1BGN7, I3LM39, Q8C6L5 and A0A0G2JVC4 have been
 893 used in the alignment. The key residues involved in the interactions are highlighted in cyan.
 894 The consensus sequence and logo representation of the residues is shown below the
 895 sequence alignment. The alignment figure was created using Jalview [33].

896

897 **Extended Data Table 1 | Cryo-EM data statistics and comparison of WT cGAS and**
 898 **cGAS (K394) structures.**

899 a, Cryo-EM data collection, refinement and validation statistics; n.a., not applicable, no
 900 model was deposited. n.a.* not applicable, a local map sharpening algorithm was used (see
 901 Methods). b, Comparison of WT-cGAS-NCP and cGAS(K394E)-NCP structures; ¹ Map-Map
 902 correlations between WT-1cGAS-1NCP and 1cGAS(K394E)-1NCP structures, and between
 903 WT-2cGAS-2NCP and 2cGAS(K394E)-2NCP structures were calculated using low-pass
 904 filtered maps (10 Å) in combination with Chimera's fit-in-map tool. ² 1cGAS(K394E)-1NCP
 905 and 2cGAS(K394E)-2NCP models were rigid-body docked into corresponding WT-cGAS-
 906 NCP maps with Chimera's fit-in-map tool (whole molecule) and B-factor refined with Rosetta.
 907 Map-Model CC was calculated with Phenix. ³ CC for cGAS chains only.

908

909

910

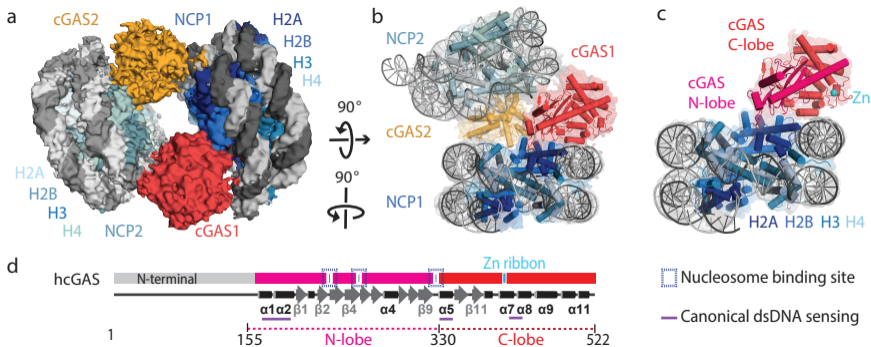
911 **References**

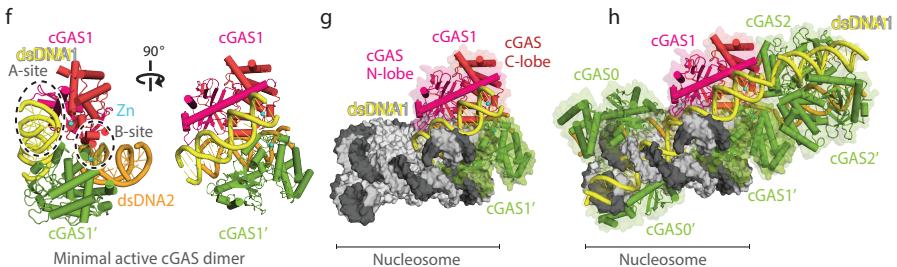
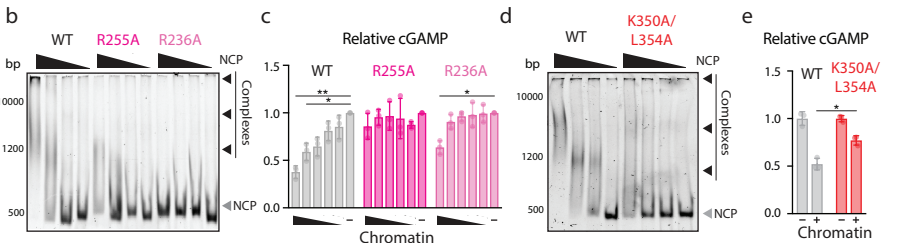
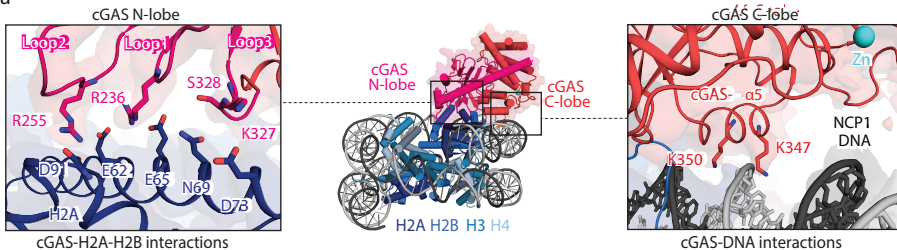
- 912 1. Ablasser, A. and Z.J. Chen, *cGAS in action: Expanding roles in immunity and*
 913 *inflammation*. Science, 2019. **363**(6431).
 914 2. Sun, L., et al., *Cyclic GMP-AMP synthase is a cytosolic DNA sensor that activates*
 915 *the type I interferon pathway*. Science, 2013. **339**(6121): p. 786-91.
 916 3. Wu, J., et al., *Cyclic GMP-AMP is an endogenous second messenger in innate*
 917 *immune signaling by cytosolic DNA*. Science, 2013. **339**(6121): p. 826-30.

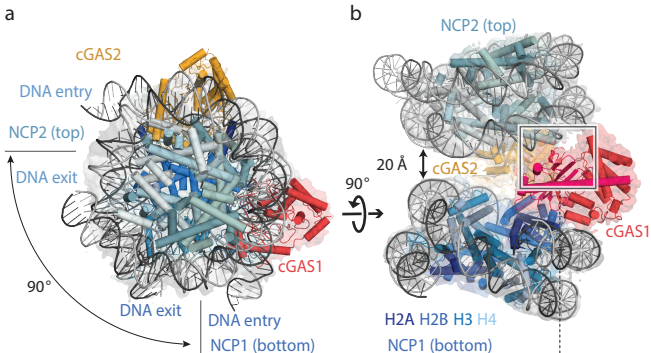
- 918 4. Ablasser, A., et al., *cGAS produces a 2'-5'-linked cyclic dinucleotide second*
919 *messenger that activates STING*. Nature, 2013. **498**(7454): p. 380-4.
- 920 5. Gao, P., et al., *Cyclic [G(2',5')pA(3',5')p] is the metazoan second messenger*
921 *produced by DNA-activated cyclic GMP-AMP synthase*. Cell, 2013. **153**(5): p. 1094-
922 107.
- 923 6. Diner, E.J., et al., *The innate immune DNA sensor cGAS produces a noncanonical*
924 *cyclic dinucleotide that activates human STING*. Cell Rep, 2013. **3**(5): p. 1355-61.
- 925 7. Zhang, X., et al., *Cyclic GMP-AMP containing mixed phosphodiester linkages is an*
926 *endogenous high-affinity ligand for STING*. Mol Cell, 2013. **51**(2): p. 226-35.
- 927 8. Gentili, M., et al., *The N-Terminal Domain of cGAS Determines Preferential*
928 *Association with Centromeric DNA and Innate Immune Activation in the Nucleus*. Cell
929 Rep, 2019. **26**(13): p. 3798.
- 930 9. Volkman, H.E., et al., *Tight nuclear tethering of cGAS is essential for preventing*
931 *autoreactivity*. Elife, 2019. **8**.
- 932 10. Barber, G.N., *STING: infection, inflammation and cancer*. Nat Rev Immunol, 2015.
933 **15**(12): p. 760-70.
- 934 11. Orzalli, M.H., et al., *cGAS-mediated stabilization of IFI16 promotes innate signaling*
935 *during herpes simplex virus infection*. Proc Natl Acad Sci U S A, 2015. **112**(14): p.
936 E1773-81.
- 937 12. Lahaye, X., et al., *NONO Detects the Nuclear HIV Capsid to Promote cGAS-*
938 *Mediated Innate Immune Activation*. Cell, 2018. **175**(2): p. 488-501 e22.
- 939 13. Zierhut, C., et al., *The Cytoplasmic DNA Sensor cGAS Promotes Mitotic Cell Death*.
940 Cell, 2019. **178**(2): p. 302-315 e23.
- 941 14. Pang, B., et al., *Drug-induced histone eviction from open chromatin contributes to the*
942 *chemotherapeutic effects of doxorubicin*. Nat Commun, 2013. **4**: p. 1908.
- 943 15. Stark, H., *GraFix: stabilization of fragile macromolecular complexes for single particle*
944 *cryo-EM*. Methods Enzymol, 2010. **481**: p. 109-26.
- 945 16. Li, X., et al., *Cyclic GMP-AMP synthase is activated by double-stranded DNA-*
946 *induced oligomerization*. Immunity, 2013. **39**(6): p. 1019-31.
- 947 17. McGinty, R.K. and S. Tan, *Nucleosome structure and function*. Chem Rev, 2015.
948 **115**(6): p. 2255-73.
- 949 18. Civril, F., et al., *Structural mechanism of cytosolic DNA sensing by cGAS*. Nature,
950 2013. **498**(7454): p. 332-7.
- 951 19. Barbera, A.J., et al., *The nucleosomal surface as a docking station for Kaposi's*
952 *sarcoma herpesvirus LANA*. Science, 2006. **311**(5762): p. 856-61.

- 953 20. Abe, T. and G.N. Barber, *Cytosolic-DNA-mediated, STING-dependent*
954 *proinflammatory gene induction necessitates canonical NF-kappaB activation*
955 *through TBK1*. J Virol, 2014. **88**(10): p. 5328-41.
- 956 21. Zhang, X., et al., *The cytosolic DNA sensor cGAS forms an oligomeric complex with*
957 *DNA and undergoes switch-like conformational changes in the activation loop*. Cell
958 Rep, 2014. **6**(3): p. 421-30.
- 959 22. Andreeva, L., et al., *cGAS senses long and HMGB/TFAM-bound U-turn DNA by*
960 *forming protein-DNA ladders*. Nature, 2017. **549**(7672): p. 394-398.
- 961 23. Zhou, W., et al., *Structure of the Human cGAS-DNA Complex Reveals Enhanced*
962 *Control of Immune Surveillance*. Cell, 2018. **174**(2): p. 300-311 e11.
- 963 24. Xie, W., et al., *Human cGAS catalytic domain has an additional DNA-binding*
964 *interface that enhances enzymatic activity and liquid-phase condensation*. Proc Natl
965 Acad Sci U S A, 2019.
- 966 25. Ablasser, A., et al., *Cell intrinsic immunity spreads to bystander cells via the*
967 *intercellular transfer of cGAMP*. Nature, 2013. **503**(7477): p. 530-4.
- 968 26. Dobbs, N., et al., *STING Activation by Translocation from the ER Is Associated with*
969 *Infection and Autoinflammatory Disease*. Cell Host Microbe, 2015. **18**(2): p. 157-68.
- 970 27. Konno, H., K. Konno, and G.N. Barber, *Cyclic dinucleotides trigger ULK1 (ATG1)*
971 *phosphorylation of STING to prevent sustained innate immune signaling*. Cell, 2013.
972 **155**(3): p. 688-98.
- 973 28. Janeway, C.A., Jr., *Approaching the asymptote? Evolution and revolution in*
974 *immunology*. Cold Spring Harb Symp Quant Biol, 1989. **54 Pt 1**: p. 1-13.
- 975 29. Ablasser, A. and S. Hur, *Regulation of cGAS- and RLR-mediated immunity to nucleic*
976 *acids*. Nat Immunol, 2020. **21**(1): p. 17-29.
- 977 30. Dolinsky, T.J., et al., *PDB2PQR: an automated pipeline for the setup of Poisson-*
978 *Boltzmann electrostatics calculations*. Nucleic Acids Res, 2004. **32**(Web Server
979 issue): p. W665-7.
- 980 31. Scheres, S.H., *RELION: implementation of a Bayesian approach to cryo-EM*
981 *structure determination*. J Struct Biol, 2012. **180**(3): p. 519-30.
- 982 32. Punjani, A., et al., *cryoSPARC: algorithms for rapid unsupervised cryo-EM structure*
983 *determination*. Nat Methods, 2017. **14**(3): p. 290-296.
- 984 33. Waterhouse, A.M., et al., *Jalview Version 2--a multiple sequence alignment editor*
985 *and analysis workbench*. Bioinformatics, 2009. **25**(9): p. 1189-91.
- 986 34. Ran, F.A., et al., *Genome engineering using the CRISPR-Cas9 system*. Nat Protoc,
987 2013. **8**(11): p. 2281-2308.
- 988 35. Haag, S.M., et al., *Targeting STING with covalent small-molecule inhibitors*. Nature,
989 2018. **559**(7713): p. 269-273.

- 990 36. Marks, B.D., et al., *Multiparameter analysis of a screen for progesterone receptor*
991 *ligands: comparing fluorescence lifetime and fluorescence polarization*
992 *measurements*. *Assay Drug Dev Technol*, 2005. **3**(6): p. 613-22.
- 993 37. Hanson, B.L., et al., *Preparation and crystallization of nucleosome core particle*.
994 *Methods Enzymol*, 2004. **375**: p. 44-62.
- 995 38. Luger, K., T.J. Rechsteiner, and T.J. Richmond, *Preparation of nucleosome core*
996 *particle from recombinant histones*. *Methods Enzymol*, 1999. **304**: p. 3-19.
- 997 39. Zhang, K., *Gctf: Real-time CTF determination and correction*. *J Struct Biol*, 2016.
998 **193**(1): p. 1-12.
- 999 40. Wagner, T., et al., *SPHIRE-crYOLO is a fast and accurate fully automated particle*
1000 *picker for cryo-EM*. *Commun Biol*, 2019. **2**: p. 218.
- 1001 41. Zivanov, J., et al., *New tools for automated high-resolution cryo-EM structure*
1002 *determination in RELION-3*. *Elife*, 2018. **7**.
- 1003 42. de la Rosa-Trevin, J.M., et al., *Xmipp 3.0: an improved software suite for image*
1004 *processing in electron microscopy*. *J Struct Biol*, 2013. **184**(2): p. 321-8.
- 1005 43. Matsumoto, S., et al., *DNA damage detection in nucleosomes involves DNA register*
1006 *shifting*. *Nature*, 2019. **571**(7763): p. 79-84.
- 1007 44. Pettersen, E.F., et al., *UCSF Chimera--a visualization system for exploratory*
1008 *research and analysis*. *J Comput Chem*, 2004. **25**(13): p. 1605-12.
- 1009 45. Emsley, P. and K. Cowtan, *Coot: model-building tools for molecular graphics*. *Acta*
1010 *Crystallogr D Biol Crystallogr*, 2004. **60**(Pt 12 Pt 1): p. 2126-32.
- 1011 46. Lowary, P.T. and J. Widom, *New DNA sequence rules for high affinity binding to*
1012 *histone octamer and sequence-directed nucleosome positioning*. *J Mol Biol*, 1998.
1013 **276**(1): p. 19-42.
- 1014 47. Adams, P.D., et al., *PHENIX: a comprehensive Python-based system for*
1015 *macromolecular structure solution*. *Acta Crystallogr D Biol Crystallogr*, 2010. **66**(Pt
1016 2): p. 213-21.
- 1017 48. Terwilliger, T.C., et al., *phenix.mr_rosetta: molecular replacement and model*
1018 *rebuilding with Phenix and Rosetta*. *J Struct Funct Genomics*, 2012. **13**(2): p. 81-90.
- 1019 49. Lebedev, A.A., et al., *JLigand: a graphical tool for the CCP4 template-restraint*
1020 *library*. *Acta Crystallogr D Biol Crystallogr*, 2012. **68**(Pt 4): p. 431-40.
- 1021 50. Davis, I.W., et al., *MolProbity: all-atom contacts and structure validation for proteins*
1022 *and nucleic acids*. *Nucleic Acids Res*, 2007. **35**(Web Server issue): p. W375-83.
1023







c

